

Deep learning waveform anomaly detector for numerical relativity catalogs

Tibério Pereira*

*Departamento de Física
Universidade Federal do Rio Grande do Norte,
Natal 59078-970, RN, Brazil*

Riccardo Sturani†

*Instituto de Física Teórica, UNESP-Universidade Estadual Paulista & ICTP South
American Institute for Fundamental Research, Sao Paulo 01140-070, SP, Brazil*

(Dated: February 22, 2024)

Numerical Relativity has been of fundamental importance for studying compact binary coalescence dynamics, waveform modelling, and eventually for gravitational waves observations. As the sensitivity of the detector network improves, more precise template modelling will be necessary to guarantee a more accurate estimation of astrophysical parameters. To help improve the accuracy of numerical relativity catalogs, we developed a deep learning model capable of detecting anomalous waveforms. We analyzed 1341 binary black hole simulations from the SXS catalog with various mass-ratios and spins, considering waveform dominant and higher modes. In the set of waveform analyzed, we found and categorised seven types of anomalies appearing in the coalescence phases.

I. INTRODUCTION

The network of gravitational wave (GW) detectors composed by the two LIGO [1] and Virgo [2] observatories has already completed three successful observation runs [3], with the detection of over 90 coalescences of compact binary systems. To maximize the possibility of detections and their (astro)physics output, collected data are analyzed via matched-filtering techniques [4, 5] by correlating them with pre-computed waveform templates, whose development is the object of intense investigation [6–12]. Improving the accuracy of GW templates straightforwardly enhances the quality of astrophysical information obtained from these sources.

Waveforms can be expressed as time series resulting from the spin-weighted spherical harmonic decomposition of the gravitational wave strain. While the dominant quadrupolar mode of GW templates has been enough to analyze the vast majority of signals, in a few cases the imprints of sub-dominant (or higher modes, HM henceforth) have been detected [13, 14]. With increasing sensitivity and widening the network of observatories in future observation runs with the KAGRA observatory [15], it is expected that HM will have a larger impact on the detected signals¹.

GW waveforms generated via Numerical Relativity (NR) simulations [17] have been widely used for construction of semi-analytical and phenomenological templates, and have produced accurate HM waveforms over a vast parameter space.

The present paper aims to provide a new tool to assess the data quality of the various waveforms presented in an NR catalog, and for the present work we focus on the SXS catalog [18]. The numerical differentiation and time integration methods can generate a systematic accumulation of numerical residue [19–21] – even more for extreme regimes such as binary black holes simulations – leading to defects in the morphology of the waveforms. Furthermore, there are cases where a catalog adds simulations with improvements in resolution (or with better numerical methods) and does not remove old simulations – because they still prove useful for theoretical studies. Hence such waveforms are the natural candidates to be identified by our tool as the ones to display inconsistencies within the catalog.

In this work, we developed the deep learning model *Waveform AnomaLy DetectOr* (WALDO), capable of signaling possible anomalous waveforms in a NR catalog [22–24]. In our searches within binary black hole (BBH) simulations, we categorized seven different types of anomalies during the stages of coalescence. Identifying and excluding such waveforms is critical to the quality of research in GW analysis and surrogate modeling [25].

Applications of deep learning models to gravitational wave data is not new [26–40], but to the best of our knowledge this is the first work using deep learning to check the consistency of numerical simulations.

The paper is structured as follows. Section II is intended to help the reader providing a reference to our notations, Section III describes the dataset we used for our analysis, and Section IV describes our machine learning-based process to identify anomalous waveforms, whose results are presented in Section V. Finally we summarize our conclusions in Section VI.

* tiberio@fisica.ufrn.br

† riccardo.sturani@unesp.br

¹ In general the predicted waveform precision requirement for real events depends on the loudness of the signal, scaling as the inverse square of its signal-to-noise ratio. For current second generation detector [16] with signal-to-noise ratio $\sim \text{few} \times 10$ a noise weighed “mismatch” of 10^{-3} is usually required.

II. DEFINITIONS

We adopt geometric units $G = c = 1$, and we denote by u the dimension-less time obtained by dividing physical time by the total mass M of the binary system, whose zero is set by the epoch of the peak of the dominant mode amplitude. The BBH mass-ratio q is taken to be larger than 1, the dimensionless spins $\vec{\chi}_i \equiv \vec{S}_i/M^2$, $i = \{1, 2\}$, being \vec{S}_i the standard spin and the orbital eccentricity is denoted by e . From the GW *strain*, i.e. the GW polarization complex combination $h_+ - ih_\times$, we extract (and rescale as usual by distance r and mass M) spherical harmonic modes $h_{lm}(t)$, indexed by integers $l \geq 2$ and $|m| \leq l$, resulting from the decomposition on the spin-weighted spherical harmonics base $_{-2}Y_{lm}$ of the strain,

$$h_{lm}(t) = \int d\Omega (h_+ - ih_\times)(\theta, \phi) {}_{-2}Y_{lm}^*(\theta, \phi), \quad (1)$$

where Ω is the solid angle parameterized by θ and ϕ , which are respectively the angle between the radiation direction and the normal to the orbital plane, and a phase corresponding to a rotation in the orbital plane.

III. THE DATASET

We create a dataset using 1341 BBH simulations from the *Simulating eXtreme Spacetimes* (SXS) catalog [17], whose parameters are in the region $q = [1.0 : 4.0]$, $|\vec{\chi}_i| = [-0.9 : 0.9]$, and $e \simeq [0.0 : 8.0 \times 10^{-4}]$ [18, 41].² All simulation names are listed in the WALDO's repository [22] (`simulations.ID.txt` file). Considering the modes ($l \leq 4$, $l-1 \leq m \leq l$)³, in total our dataset is composed by $N_d = 6 \times 1341 = 8046$ waveforms. Figure 1 shows the parameter space distribution of eccentricity, spin-aligned parameter χ_{eff} [42] spin-precession parameter χ_p [43] and the mass-ratio $q > 1$, highlighting the simulations showing anomalies (discussed in the Section V). The spin parameters $\chi_{eff,p}$ are approximately constant even in the case of precession, so they are particularly useful in characterizing the waveform parameter space. Their explicit expressions are

$$\begin{aligned} \chi_{eff} &\equiv \frac{S_{1\parallel}/m_1 + S_{2\parallel}/m_2}{m_1 + m_2}, \\ \chi_p &\equiv \frac{\max(A_1 S_{1\perp} + A_2 S_{2\perp})}{A_2 m_2^2}, \end{aligned} \quad (2)$$

where $S_{i\parallel,\perp}$ denote the spin component of the i -th binary constituent respectively parallel and perpendicular to the

Newtonian orbital angular momentum, with $A_i \equiv 2 + 3m_i/(2m_{j \neq i})$.

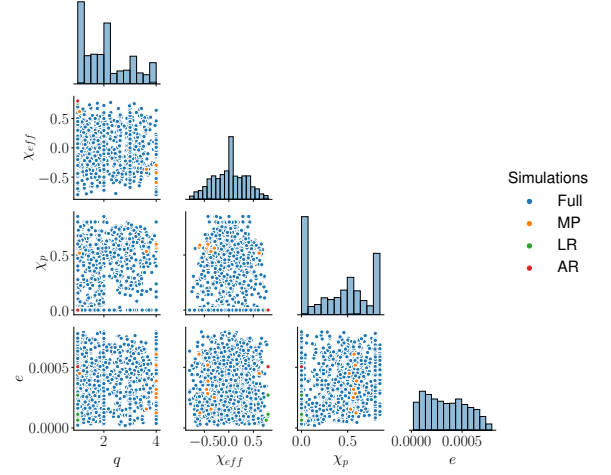


FIG. 1. Representation of the parameter space of the 1341 simulations: corner plot of the distribution of eccentricity e , mass-ratio q , spin-aligned parameter χ_{eff} and spin-precession χ_p , defined in Sec. III. We highlighted the waveforms presenting the anomalies displayed in the list on the right of the figure, whose acronyms are defined in Tab. I.

To facilitate a unified treatment of all waveforms, we cut the waveforms to the highest initial time value of the entire dataset, i.e., the inspiral starts at $u = -1700$, with corresponding instantaneous frequency for the dominant mode $f_{min} \simeq 14 - 19Hz (M/100M_\odot)^{-1}$, depending on the mass ratio. This conditioning is necessary to guarantee the same resolution of the waveforms – with the same time intervals – during the neural network (NN) training⁴.

Also, we find it convenient to re-sample all modes via the time-reparametrization

$$\begin{aligned} u'(u) &= c_1 r(u) + c_2, \\ r(u) &= \tanh[a(u - u_0 + b)], \\ c_1 &= (u_F - u_0) / [r(u_F) - r(u_0)], \\ c_2 &= u_0 - c_1 r(u_0), \end{aligned} \quad (3)$$

where u_0 and u_F are the initial and final value of the dimension-less time $u = [-1700 : 100]$; $a = 5.0 \times 10^{-4}$ and $b = 5.0 \times 10^2$ are constants, see e.g. [44] for analog reparametrization. The rationale for this parameterization is to make smoother the transition from the wider spacing during the inspiral to a smaller one in the merger-ringdown phase, while keeping the number of samples equal to $N_s = 2048$ for all waveforms, without degrading the sampling rate in the merger-ringdown phase. This

² We restricted our analysis to the 1341 simulations with mass ratio $q \leq 4$ because beyond this value simulations become sparser, and this can jeopardize the learning process of the neural network model training.

³ To make it explicit, we use the $(2, 2)$, $(2, 1)$, $(3, 3)$, $(3, 2)$, $(4, 4)$, $(4, 3)$, i.e., 6 modes for each simulation in the catalog.

⁴ For all numerical waveforms we used the best resolution available in the repository.

reparameterization does not bring morphological issues or degenerate the accuracy of the waveforms, but it helps the NN to capture more precise features after the inspiral.

For deep learning *feature engineering* – the pre-processing procedures for improving NN computations – we normalize the entire dataset with the highest peak value among all waveform amplitudes,

$$h_{k,lm} \rightarrow h_{k,lm} / \max(A_k), \quad (4)$$

where the index (k) denotes the simulation number, $k = [1 : 1341]$, and A_k is the dominant mode maximum amplitude value of the k -th simulation. We define the dataset as the numerical three-dimensional array,

$$\mathbf{X} \equiv (\text{Re}\{h_{k,lm}\}, \text{Im}\{h_{k,lm}\}), \quad (5)$$

whose dimensionality is $(N_d, N_s, 2)$.

IV. WALDO

The Waveform AnomaLy DetectOr (WALDO) holds a U-Net architecture [45], where the waveform input $X_{k,lm}$ is reproduced as the output $\bar{X}_{k,lm}$. During the training, the model learns all possible waveform features related to the parameter space. Evaluating its performance after training with the *mismatch* \mathcal{M} between $h_{k,lm}$ and its prediction $\bar{h}_{k,lm}$, the measurement of high mismatch values can flag the presence of waveforms whose morphology do not match the dataset one, *i.e.*, we can find *anomalous waveforms*. The mismatch is defined as $\mathcal{M} \equiv 1 - \mathcal{O}$, where \mathcal{O} denotes the *match* between two time series $h_{1,2}$, defined in terms of the scalar product

$$\langle h_1 | h_2 \rangle = 4 \int_0^\infty \frac{\tilde{h}_1(f) \tilde{h}_2^*(f)}{S_n(f)} df, \quad (6)$$

where f is variable conjugate to time under Fourier transform $h \rightarrow \tilde{h}$, and $S_n(f)$ is the noise spectral density – we set $S_n(f) = 1$ for noise-free waveforms. The match being defined by maximization over initial phase and time of the scalar product of normalized waveforms

$$\mathcal{O} \equiv t, \phi_0 \frac{\langle h_1 | h_2 \rangle}{(\langle h_1 | h_1 \rangle \langle h_2 | h_2 \rangle)^{1/2}}. \quad (7)$$

The WALDO's architecture is illustrated in Fig. 2, where the input for one waveform, addressed by Eq. 5, undergoes a succession of convolution and max-pooling operations given by the solid right and down arrows, respectively. Those operations in the encoder part (the left-hand side blocks) use a one-dimensional kernel/window to sweep the time series and make operations for output. We adopt a *kernel-size* = 3 for convolutional layers and the respective number of kernels C per encoder layer as $C = [32, 64, 128, 256, 512]$. For the max-pooling layers, we use a *pool-size* = 2 to halve the time series size (by

taking the maximum value between two points) as the number of convolutional kernels increases to improve the feature extraction.

The model's decoder part (the right-hand side blocks) doubles the time series size with up-sampling layers, indicated by up arrows. It concatenates their outputs with the encoder layer with the corresponding dimensions, shown by dashed right arrows and blocks. These operations follow a convolutional layer which reduces the number of kernels. In short, the decoder blocks restore the input X original dimension meanwhile transfer the encoder features to improve \bar{X} resolution. We compose the whole architecture with ReLU activation functions except for the hyperbolic tangent in the output layer.

An unsupervised model for the anomaly detection task usually uses an auto-encoder architecture, a structure similar to the scheme of Fig. 2 but without the connections represented by the dashed arrows. In the U-Net model, these connections help the convolutional layers of the decoder to reproduce the kernels that best extract the features in the encoder blocks. Therefore, the U-Net model can perform better in waveform reproduction than a conventional autoencoder model for a reduced dataset. This choice with the Adagrad optimizer allows a smooth minimization of the loss function and high resolution waveform reproduction.

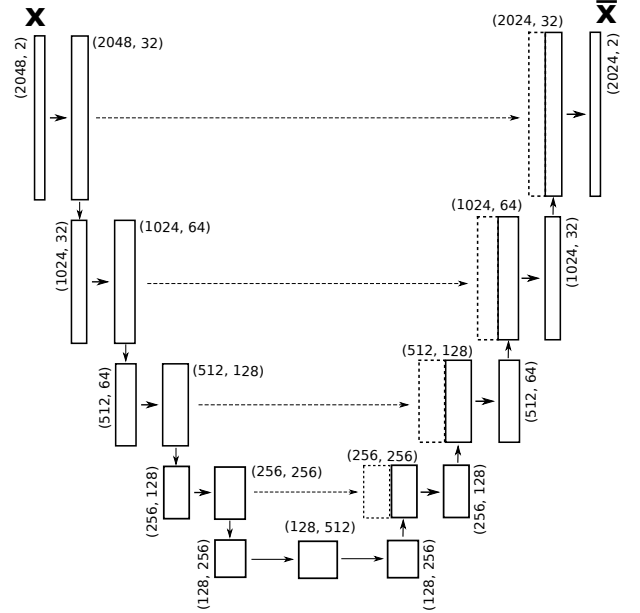


FIG. 2. Illustration of the WALDO's U-Net architecture.

A. Training and validation

To examine the training performance, we split the dataset into 90% for training and validation data and 10% for testing data. Since 8046 waveforms form a small dataset, we use the *K-fold validation* method for $K = 3$

and $batch-size = 1$. We optimize the model parameters using the mean squared error (MSE) loss function and Adagrad optimizer [46]. During the validation, the NN can be trained through 200 epochs without over-fitting since we applied an early-topping mechanism to prevent the training for the difference of train and validation losses greater than 1.0×10^{-8} . We retrain the model using 90% of the dataset and obtain the MSE average of 2.8×10^{-7} over the testing data. Figure 3 shows the training and validation performance with, respectively, solid and dashed lines per each fold-validation.

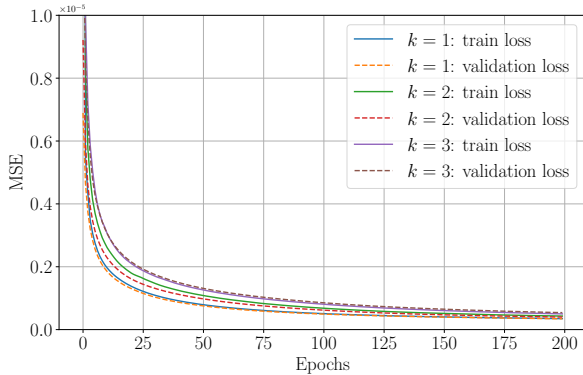


FIG. 3. The mean squared error (MSE) evaluation over 200 epochs in 3-fold validation performance. Solid lines represent the training loss, while dashed ones show the validation loss.

V. RESULTS

After the training, WALDO evaluates the mismatch and packs the values with (l, m) mode labels, together with the identification simulation number (ID) – that comes from the SXS simulation names as SXS:BBH:ID – the parameter space $(q, \vec{\chi}_1, \vec{\chi}_2, e)^{(k)}$, the waveforms $h_{k,lm}$ and their predictions $\bar{h}_{k,lm}$. Creating a histogram for each mode (l, m) , we isolated 1% of the highest mismatch waveforms to verify any possible morphological discrepancy in the predictions. Figure 4 shows the $(3, 2)$ waveform mismatch distribution of average 1.26×10^{-5} represented by the vertical green line; the $quantile = 0.99$, marked by the vertical pink line, separates 14 simulations that call for examination. The lowest mismatch value is on the order of 5.0×10^{-6} due to the low number of simulations $N_d = 1341$ and varied waveform morphology. We reinforce that the NN training is usually done with hundreds of thousands of data; however, our small dataset does not interfere with the quality of waveform reproduction once our NN model achieved a mismatch average of 1.25×10^{-5} , while the SXS threshold accuracy is 1.0×10^{-5} times above the amplitude peak [47].

In this case, we found high mismatches due to noise accumulation in the predicted waveforms, even if qualitatively they follow the NR morphological patterns, as

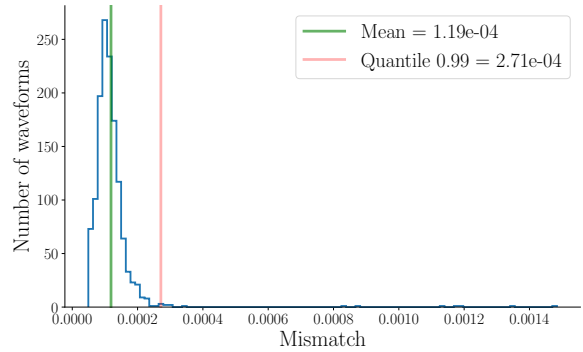


FIG. 4. Mismatch histogram of 1341 waveforms $h_{32}^{(k)}$ and the predictions $\bar{h}_{32}^{(k)}$. The vertical green line shows the average value 1.26×10^{-5} , and the pink one marks the $quantile = 0.99$ with 14 simulations on its right side.

shown in Fig. 5 – where the blue line is h_{32} , the dashed orange line is \bar{h}_{32} , and the green one is $Re\{h_{32} - \bar{h}_{32}\}$ amplified 10 times. On the other hand, we also found morphological discrepancies between NN predicted and NR waveform modes, confined in specific sectors of the coalescence, causing high mismatches.

An irregularity fairly common for the higher modes shows that the mode amplitude around the merger peak has a greater magnitude than expected – what we call the *merger-peak* (MP) anomaly, as seen in Fig. 6.

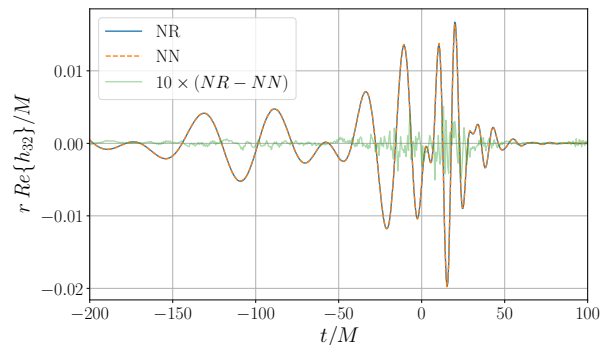


FIG. 5. NR vs NN comparison of the $(3, 2)$ -waveforms from the simulation ID = 1018. $Mismatch = 3.0 \times 10^{-4}$; $q = 1.2$, $\vec{\chi}_1 = (-0.59, 0.15, -0.39)$, $\vec{\chi}_2 = (-0.73, 0.19, 0.22)$, and $e = 4.2 \times 10^{-4}$.

For even m modes, we found MP anomalies in $ID_{(3,2)} = [1863, 1991 - 1993, 1995]$ and $ID_{(4,4)} = [1982, 1983, 1991, 1992, 1995]$. In the search for odd m modes, we restrict the mass ratio to $q > 1.0$, where we found $ID_{(2,1)} = [1982, 1993]$, $ID_{(3,3)} = [1982, 1983, 1989, 1991 - 1993, 1995]$, and $ID_{(4,3)} = [0601, 1982, 1983, 1989, 1991 - 1993, 1995]$.

In some waveform $(4, 4)$ modes the ringdown decay begins a little later in NR simulations than in our

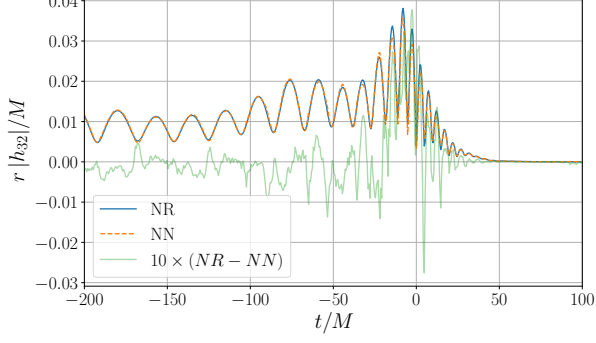


FIG. 6. NR vs NN comparison of the (3, 2)-waveforms from the simulation ID = 1995, displaying a MP anomaly. $Mismatch = 1.48 \times 10^{-3}$; $q = 4.0$, $\vec{\chi}_1 = (0.51, -0.29, -0.54)$, $\vec{\chi}_2 = (0.07, 0.07, -0.79)$, and $e = 1.2 \times 10^{-4}$.

NN predictions. Figure 7 shows an example of the *lazy-ringdown* (LR) anomaly, also found in $ID_{(4,4)} = [0230, 1477, 1481, 2104]$. In the simulation $ID_{(4,4)} = 0155$, on the other hand, the ringdown amplitude does not exhibit appropriate asymptotic behavior. The *asymptotic-ringdown* (AR) anomaly is shown in Fig. 8.

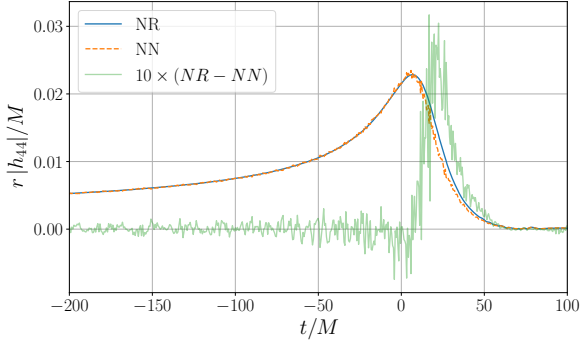


FIG. 7. NR vs. NN comparison of the (4, 4)-waveforms from the simulation ID = 0328 displaying a LR anomaly. $Mismatch = 1.44 \times 10^{-3}$; $q = 1.0$, $\vec{\chi}_1 = (0.0, 0.0, 0.8)$, $\vec{\chi}_2 = (0.0, 0.0, 0.8)$, and $e = 1.1 \times 10^{-4}$.

Figure 1 shows the parameter space corner plot of all simulations as blue dots, highlighting the simulations with Merger-Peak (MP, orange), Lazy-Ringdown (LR, green), and Asymptotic-Ringdown (AR, red). We can notice that we only have AR and LR anomalies in the very boundary of the parameter space. To check whether these anomalies are due to the NN learning bias, we constrain the search in the dataset for further analysis.

A. Constrained dataset search

The homogeneity of the parameter space distribution is important to avoid WALDO prediction bias. For

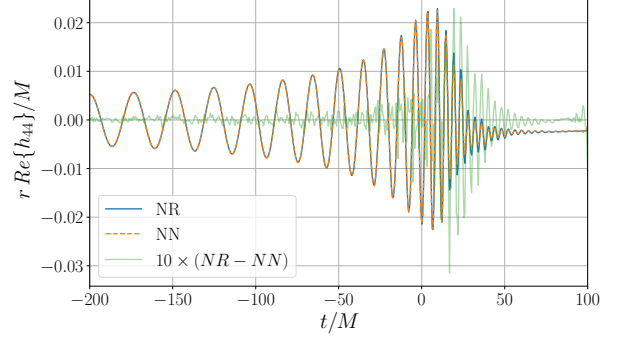


FIG. 8. NR vs. NN comparison of the (4, 4)-waveforms from the simulation ID = 0155 exemplifying a AR anomaly. $Mismatch = 1.21 \times 10^{-3}$; $q = 1.0$, $\vec{\chi}_1 = (0.0, 0.0, 0.8)$, $\vec{\chi}_2 = (0.0, 0.0, 0.8)$, and $e = 5.1 \times 10^{-4}$.

instance, a dataset containing 500 simulations of spin-aligned BBH and 20 precessing binaries can lead to high mismatch values for waveforms whose features indicate precession.

Thereby, we focus our search for anomalies on $|\vec{\chi}_{1,2}| \leq 0.4$ – but keeping the same training set – where we have a higher simulation density. We choose *quantile* = 0.90 to isolate 15 waveforms. This constraint leads us to find more AR anomalies in $ID_{(3,3)} = [0116, 0115, 0119, 0129]$ and $ID_{(4,4)} = [0070, 0115, 0124, 0135, 0150]$. In addition, we found waveforms with similar decay as in Fig. 8, but with non-oscillatory patterns. In this case, those ringdowns were affected by the time interpolation of Eq. 3 because their final time is smaller than $u = 70$, giving rise to what we dubbed *short-ringdown* (SR) anomaly, found in $ID_{(l,m)} = [1112, 1114, 1133]$, for all (l, m) . Fig. 9 shows the h_{22} modes from these simulations.

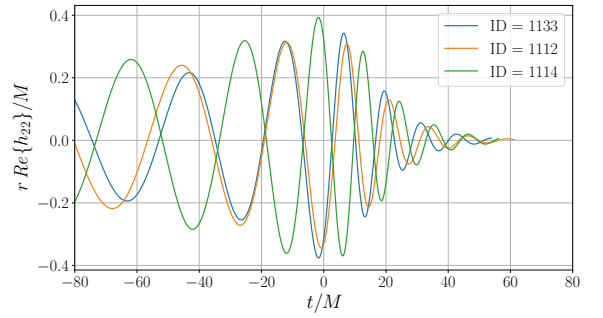


FIG. 9. Short-ringdown anomaly in the simulations ID = [1112, 1114, 1133].

The ringdown amplitude of the dominant mode is expected to show a smooth, quasi-exponential decay, however, in the simulations $ID_{(2,2)} = [0066, 0067, 0070, 0072, 0126, 0136]$ appear small ripples up to $u = 40$ as in Fig. 10, which we call the *rippled-ringdown* (RR) anomaly.

Note that these small ripples are present in several of the original NR simulations, and they are reproduced by the NN predictions, however with high enough mismatch to be uncovered.

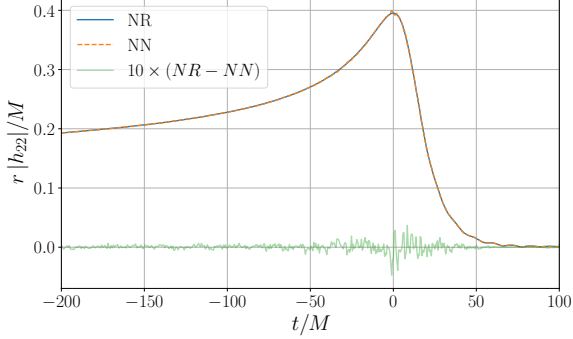


FIG. 10. NR vs. NN comparison of the (2, 2)-waveforms from the simulation ID = 0072, showing a RR anomaly. $Mismatch = 1.33 \times 10^{-5}$; $q = 1.0$, $\vec{\chi}_1 = (0.0, 0.0, 0.0)$, $\vec{\chi}_2 = (0.0, 0.0, 0.0)$, and $e = 1.5 \times 10^{-4}$.

The simulations analyzed in the constrained search are not on the parameter space boundary we chose (apart from the $q = 1$ physical boundary), see Fig. 11. By focusing on our previously defined constrained set of parameters, the AR anomalies are the only ones which are carried over from previous analysis, indicating that their presence is not due to NN learning bias due to parameter space boundaries.

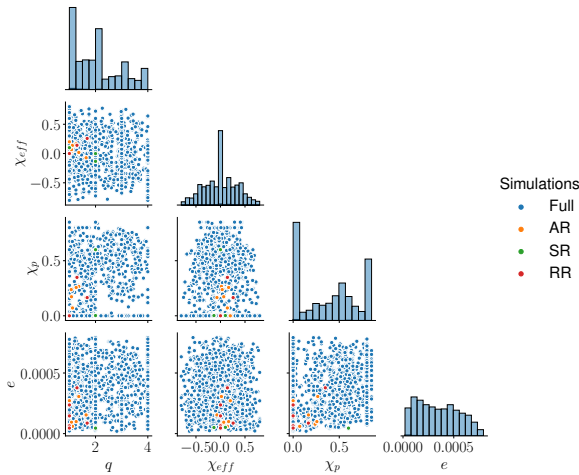


FIG. 11. Analog to Fig. 1, but highlighting only the anomalies of the constrained search of the waveforms, see Tab. I for acronyms.

B. Radiation field search

In NR the strain modes are usually computed by the integration of the radiation field Ψ_4 [48], or independently, via perturbative formulation of the metric – the Regge-Wheeler-Zerilli formalism used in SXS simulations [49, 50]. We investigate the $\psi_{lm} = \ddot{h}_{lm}$ time series within the whole dataset to ensure the quality of both strain and Ψ_4 modes.

We retrained the NN, using the same architecture setup as before and training time, and evaluate the mismatch between NR $\psi_{k,lm}$ waveforms and their reproductions $\bar{\psi}_{k,lm}$.

From previous analyses, we found exclusively MP anomalies in ψ_{lm} modes in $ID_{(2,2)} = [1993, 1995]$, $ID_{(3,2)} = [1863, 1878, 1983, 1991 - 1993, 1995]$, $ID_{(3,3)} = [1982, 1989, 1991 - 1993]$, $ID_{(4,3)} = [1103, 1982, 1983, 1989, 1991 - 1993]$, and $ID_{(4,4)} = [0024, 0126, 1982, 1989, 1993, 1995]$. Some of these simulations listed are the same as those in the previous h_{lm} waveform analysis.

Still, some ψ_{lm} modes revealed smaller amplitude magnitudes than the predictions, in the initial region of the merger, as seen in Fig. 12. These *initial-merger* (IM) anomalies are present in ψ_{lm} with $ID_{(2,2)} = [1982, 1989]$, $ID_{(3,2)} = [1982, 1989]$, $ID_{[(3,3), (4,3), (4,4)]} = 1995$.

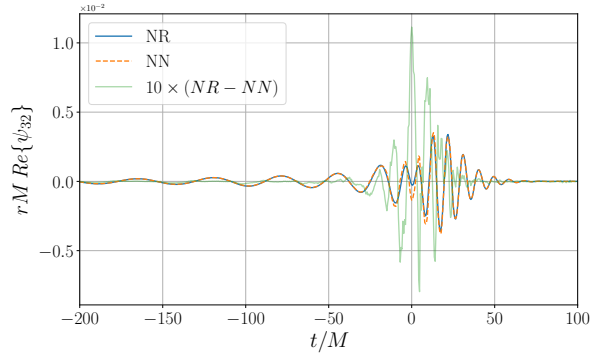


FIG. 12. NR vs NN comparison of the ψ_{32} from the simulation ID = 1989. $Mismatch = 2.7 \times 10^{-3}$; $q = 4.0$, $\vec{\chi}_1 = (-0.50, -0.29, -0.55)$, $\vec{\chi}_2 = (0.02, -0.10, -0.79)$, and $e = 6.1 \times 10^{-4}$.

In the ψ_{lm} mode (2,1), we did not find MP or IM anomalies but discrepancies between NR and NN waveforms in phase and amplitude of the inspiral region in $ID_{(2,1)} = [0013, 0252, 0292, 0388, 0513, 0464, 1508, 2126]$. The dephased-inspiral (DI) anomaly, as seen in Fig. 13, occurs in non-precessing binaries, in which we do not expect such oscillations in the waveform inspiral amplitudes. In this figure, we decreased the transparency of the NN prediction for better visualization of the oscillations between $[-400 : -80]t/M$ in the NR waveform amplitude. This particular set of simulations was found with eccentricity $e > 10^{-4}$.

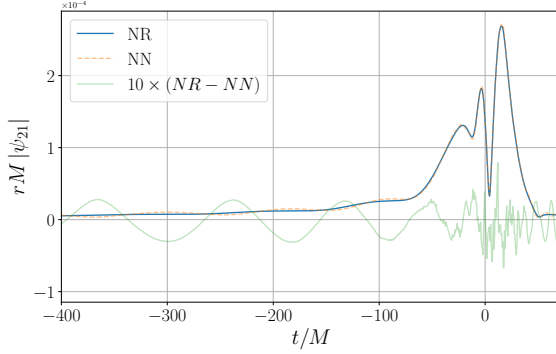


FIG. 13. NR vs NN comparison of the ψ_{21} from the simulation ID = 0292, showing a DI anomaly. $Mismatch = 3.87 \times 10^{-3}$; $q = 3.0$, $\vec{\chi}_1 = (0.0, 0.0, 0.73)$, $\vec{\chi}_2 = (0.0, 0.0, -0.85)$, and $e = 1.5 \times 10^{-4}$.

The results of the anomaly search presented in this subsection are summarized in Fig. 14, where IM anomaly appears only for $q = 4$, *i.e.*, at the boundary of our waveform sample, and DI anomaly is present only in non-precessing binaries which makes stronger the case for an actual anomaly.

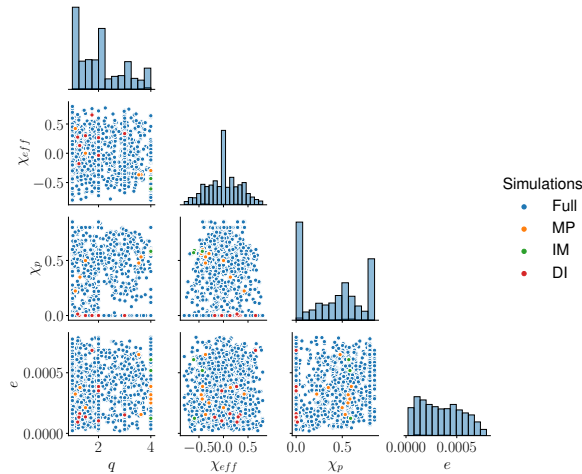


FIG. 14. Analog to Fig. 1 and 11, but highlighting only the anomalies of the ψ_4 set, see Tab. I for acronyms.

C. Anomaly detection statistics

The anomalous waveforms found are mostly local morphological defects that differ from the waveform reproduced by WALDO as in Fig. 12. Still, we want to know whether our model has learned the waveform features corresponding to the entire parameter space of Fig. 1 or it is creating such anomalies. For this, we simulate fake waveforms and check whether WALDO evaluates them

as outliers.

To generate a fake waveform, we inject a Gaussian noise $n(t)$ of size N_t into a randomly chosen h_{lm} waveform from the dataset. So, we calculate the signal-to-noise ratio (SNR) from the signal $s_{lm} = h_{lm} + n$ as follows

$$SNR_n = \frac{\langle h_{lm} | s_{lm} \rangle}{\langle h_{lm} | h_{lm} \rangle^{1/2}}, \quad (8)$$

this time estimating the spectral noise density S_n of n and using it in the definition (Eq. 6) for the scalar product. All “fake” waveforms will receive the SNR value, in large, together with their ID number so that we can identify them after the mismatch evaluation.

We adopt an SNR_n range $[1.0 : 10.0] \times 10^3$ for the experiment. Figure 15 shows an example of a waveform with noise (dashed orange line) and without noise (blue line), for $SNR_n = 1000.0$ on the plot above and $SNR_n = 5500.0$ on the plot below.

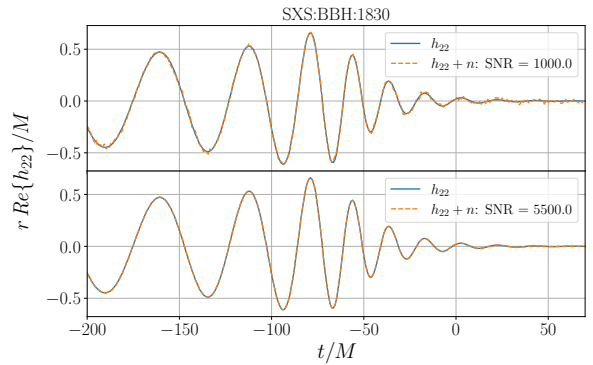


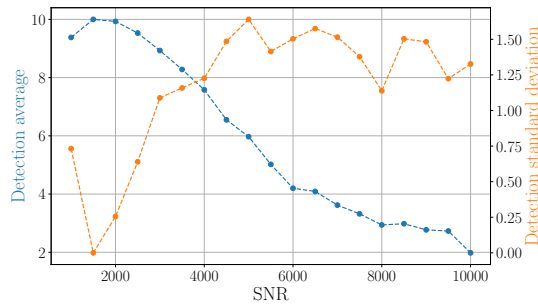
FIG. 15. Waveform h_{22} (blue line) from SXS:BBH:1830 simulation. The plot above shows the noise injection of $SNR_n = 1000.0$; below, an injection of $SNR_n = 5500.0$ (dashed orange lines).

To guarantee a dataset free from anomalous waveforms, we kept 30% of the best waveforms of each mode (l, m) , which formed the *clean-dataset* with 2904 waveforms. We inject noise into 10 waveforms from the clean-dataset at random. With WALDO trained on the original dataset, we evaluate the clean-dataset and separate 5% of the highest mismatch waveforms (18 outliers). Next, we compute how many waveforms from the 10 fake ones appeared among the 18 outlier waveforms.

This experiment was repeated 100 times so that we have, in Fig. 16, the mean amount (left-hand side y-axis and blue line) and standard deviation (right-hand side y-axis and orange line) of fake waveforms found per each SNR_n value. This result indicates that WALDO starts to present a doubtful detection (average of false waveforms found equal to 5 out of 10) for $SNR_n \geq 5500.0$ (see fake waveform in the plot below of Fig. 16).

Anomaly	Description
(AR) Asymptotic-Ringdown	Non-null asymptotic behavior during ringdown.
(LR) Lazy-Ringdown	Ringdown late decay.
(RR) Rippled-Ringdown	Ripples in the dominant mode ringdown amplitude.
(SR) Short-Ringdown	Ringdown with length below $70M$.
(MP) Merger-Peak	Higher amplitude around the merger peak.
(IM) Initial-Merger	Shorter amplitude in the merger beginning.
(DI) Dephased-Inspiral	Oscillatory dephasing during inspiral.

TABLE I. Seven waveform anomalies detected by WALDO.

FIG. 16. Detection average (blue line) and standard deviation (orange line) of fake waveforms per SNR_n value.

VI. DISCUSSION

To assess the quality of Numerical Relativity data, and to identify problematic waveform candidates, we developed the Waveform AnomaLy DetectOr (WALDO) which allowed us to identify potentially anomalous waveforms both in the dominant and higher modes. We trained our model with 8046 waveforms – considering the SXS center of mass (CoM) correction and the outermost extraction – with a U-Net neural architecture and calculated the mismatch between the NR waveforms and the NN predictions. By isolating the 1% waveforms with highest mismatch, we identified seven qualitatively different anomalies during the inspiral, merger, and ringdown stages. Table I summarizes the anomaly categories.

We focus our anomaly search on the *quantile* > 0.99 region of the mismatch, and for higher modes with $(l \leq 4, l - 1 \leq m \leq l)$.

The different anomalies found by WALDO are *potential* inaccuracies in the waveform extraction or numerical evolution of field equations. We are not pointing out these simulations as definitively incorrect, but we are discussing a way to assess the quality of these data to identify a small subset of the entire waveform catalog which may deserve a closer scrutiny.

While lacking analytic approximation approaches to check the consistency of the NR waveforms, as they only cover the inspiral and ringdown stages separately, we believe that the complete evaluation of the coalescence phases would only be possible – as far as we know – by

correlating NR waveforms from different catalogs, which seems impractical.

We highlighted seven types of anomalous NN reconstructions whose patterns repeated for different simulations. From those, four types are undoubtedly morphological anomalies from simulation issues:

1. Asymptotic-Ringdown – all ringdown waveform amplitudes from a compact binary coalescence source go asymptotically to zero around 100 solar mass after the amplitude peak;
2. Short-Ringdown – they are anomalous simulations concerning the catalog since they finish too early to complete an asymptotically zero amplitude;
3. Rippled-Ringdown – the ringdown amplitude of the dominant mode is analytically expected to decay smoothly, without mode mixing;
4. Dephased-Inspiral – found in ψ_{21} waveforms, seems to be a mode mixing effect due to the binary CoM drift caused by the residual momentum of the simulation’s initial condition [48]. We stress that oscillations qualitatively similar to the ones in Fig. 13, while should not appear in non-precessing waveforms, are common in precessing ones, which are the majority in the catalog. Hence it is likely that NN learned from precessing waveforms to reproduce amplitude oscillations and output it also in a non-precessing case.

The three remaining anomalies (Merger-Peak, Initial-Merger, and Lazy-Ringdown) are very local patterns in the merger-ringdown phases. IM and LR are the only two cases with simulations in the boundary of some parameter range: IM for equal masses and spin-aligned BBHs; and LR for mass-ratio $q = 4$, but varied spin values. Since we found four different types of anomalies using our methodology, we could not fail to show these other three discrepancies between NR and NN waveforms.

We calculated the average of fake waveform detections created by noise injection (Sec. V C) for a statistical analysis of the anomalous waveform detection. This result indicates that the limit of the detection performance is for $SNR_n \geq 5500.0$, which are fake waveforms with negligible noise (see Fig. 15).

The use of machine learning can be a great ally to extracting catalog features and reproducing waveforms

with confidence. The present work intends to be a starting point for a more thorough investigation of NN applied to numerical waveforms.

As most of the anomalies appeared during the merger-ringdown stages, this may suggest the need for improvement of the *adaptive mesh refinement* method of numerical simulations [21]. Since the more refined the calculations during the collision of black holes, the more accurate the waveform during the merger.

We stress that for our analysis the dataset need to be as homogeneous as possible in terms of astrophysical parameter space, to avoid large mismatch values when dealing with anomaly-free waveforms because of poor modeling. It is essential to remove simulations that have anomalies from the dataset and re-train the NN to ensure that low-quality simulations do not pollute the training set. Such anomalies can impair waveform modeling [51–54] and interfere with analysis, such as the ringdown quasi-normal modes [55–57].

We propose that WALDO can be applied to any time series, such as gravitational waves from binary neutron

star and back hole-neutron star binary. Also, we suggest to evaluate the quality of new simulations for the next generations of NR codes by comparing them with waveforms from well-established catalogs in the literature.

ACKNOWLEDGMENTS

The authors thank the International Institute of Physics for hospitality and support during most of this work. We thank Michael Boyle, from the SXS team, for the valuable discussions. TP is supported by the Coordenação de Aperfeiçoamento de Pessoal de Nível Superior (CAPES) – Graduate Research Fellowship. The work of RS is partly supported by CNPq under grant 310165/2021-0 and RS would like to thank ICTP-SAIFR FAPESP Grant No. 2016/01343-7. The authors thank the High Performance Computing Center (NPAD) at UFRN for providing the computational resources necessary for this work.

-
- [1] J. Aasi *et al.* (LIGO Scientific), *Class. Quant. Grav.* **32**, 074001 (2015), arXiv:1411.4547 [gr-qc].
 - [2] F. Acernese *et al.* (VIRGO), *Class. Quant. Grav.* **32**, 024001 (2015), arXiv:1408.3978 [gr-qc].
 - [3] R. Abbott *et al.* (LIGO Scientific, VIRGO, KAGRA), (2021), arXiv:2111.03606 [gr-qc].
 - [4] L. A. Wainstein and V. D. Zubakov, *Extraction of Signals from Noise*, Dover books on physics and mathematical physics (Prentice-Hall, Englewood Cliffs, NJ, 1962).
 - [5] B. P. Abbott *et al.* (LIGO Scientific, Virgo), *Class. Quant. Grav.* **37**, 055002 (2020), arXiv:1908.11170 [gr-qc].
 - [6] G. Pratten *et al.*, *Phys. Rev. D* **103**, 104056 (2021), arXiv:2004.06503 [gr-qc].
 - [7] G. Pratten, S. Husa, C. Garcia-Quiros, M. Colleoni, A. Ramos-Buades, H. Estelles, and R. Jaume, *Phys. Rev. D* **102**, 064001 (2020), arXiv:2001.11412 [gr-qc].
 - [8] C. García-Quirós, S. Husa, M. Mateu-Lucena, and A. Borchers, *Class. Quant. Grav.* **38**, 015006 (2021), arXiv:2001.10897 [gr-qc].
 - [9] C. García-Quirós, M. Colleoni, S. Husa, H. Estellés, G. Pratten, A. Ramos-Buades, M. Mateu-Lucena, and R. Jaume, *Phys. Rev. D* **102**, 064002 (2020), arXiv:2001.10914 [gr-qc].
 - [10] S. Ossokine *et al.*, *Phys. Rev. D* **102**, 044055 (2020), arXiv:2004.09442 [gr-qc].
 - [11] S. Babak, A. Taracchini, and A. Buonanno, *Phys. Rev. D* **95**, 024010 (2017), arXiv:1607.05661 [gr-qc].
 - [12] Y. Pan, A. Buonanno, A. Taracchini, L. E. Kidder, A. H. Mroué, H. P. Pfeiffer, M. A. Scheel, and B. Szilágyi, *Phys. Rev. D* **89**, 084006 (2014), arXiv:1307.6232 [gr-qc].
 - [13] R. Abbott *et al.* (LIGO Scientific, Virgo), *Phys. Rev. D* **102**, 043015 (2020), arXiv:2004.08342 [astro-ph.HE].
 - [14] R. Abbott *et al.* (LIGO Scientific, Virgo), *Astrophys. J. Lett.* **896**, L44 (2020), arXiv:2006.12611 [astro-ph.HE].
 - [15] H. Abe *et al.* (KAGRA), *Galaxies* **10**, 63 (2022).
 - [16] M. Pürrer and C.-J. Haster, *Phys. Rev. Res.* **2**, 023151 (2020), arXiv:1912.10055 [gr-qc].
 - [17] M. A. Scheel, M. Boyle, T. Chu, L. E. Kidder, K. D. Matthews, and H. P. Pfeiffer, *Phys. Rev. D* **79**, 024003 (2009).
 - [18] M. Boyle *et al.*, *Class. Quant. Grav.* **36**, 195006 (2019), arXiv:1904.04831 [gr-qc].
 - [19] M. Boyle, L. Lindblom, H. Pfeiffer, M. Scheel, and L. E. Kidder, *Phys. Rev. D* **75**, 024006 (2007), arXiv:gr-qc/0609047.
 - [20] O. Rinne, L. Lindblom, and M. A. Scheel, *Class. Quant. Grav.* **24**, 4053 (2007), arXiv:0704.0782 [gr-qc].
 - [21] B. Szilágyi, *International Journal of Modern Physics D* **23**, 1430014 (2014).
 - [22] T. Pereira, “Waveform AnomaLy DetectOr (WALDO),” (2022).
 - [23] “Waveform anomaly detector,” https://github.com/tiberioap/grav_waldo, accessed: 2023-12.
 - [24] “Waveform anomaly detector,” <https://ascl.net/2301.021>, accessed: 2023-12.
 - [25] V. Varma, S. E. Field, M. A. Scheel, J. Blackman, D. Gerosa, L. C. Stein, L. E. Kidder, and H. P. Pfeiffer, *Phys. Rev. Research* **1**, 033015 (2019), arXiv:1905.09300 [gr-qc].
 - [26] P. J. Easter, P. D. Lasky, A. R. Casey, L. Rezzolla, and K. Takami, *Phys. Rev. D* **100**, 043005 (2019), arXiv:1811.11183 [gr-qc].
 - [27] H. Gabbard, M. Williams, F. Hayes, and C. Messenger, *Physical Review Letters* **120** (2018), 10.1103/physrevlett.120.141103.
 - [28] V. Varma, D. Gerosa, L. C. Stein, F. Hebert, and H. Zhang, *Phys. Rev. Lett.* **122**, 011101 (2019), arXiv:1809.09125 [gr-qc].
 - [29] H. Shen, D. George, E. A. Huerta, and Z. Zhao, in *ICASSP 2019 - 2019 IEEE International Conference on Acoustics, Speech and Signal Processing (ICASSP)* (IEEE, 2019).
 - [30] A. Rebei, A. Huerta, S. Wang, S. Habib, R. Haas,

- D. Johnson, and D. George, *Physical Review D* **100** (2019), 10.1103/physrevd.100.044025.
- [31] Y. Setyawati, M. Pürrier, and F. Ohme, *Class. Quant. Grav.* **37**, 075012 (2020), arXiv:1909.10986 [astro-ph.IM].
- [32] L. Haegel and S. Husa, *Class. Quant. Grav.* **37**, 135005 (2020), arXiv:1911.01496 [gr-qc].
- [33] E. Cuoco *et al.*, *Mach. Learn. Sci. Tech.* **2**, 011002 (2021), arXiv:2005.03745 [astro-ph.HE].
- [34] S. R. Green, C. Simpson, and J. Gair, *Physical Review D* **102** (2020), 10.1103/physrevd.102.104057.
- [35] R. Ormiston, T. Nguyen, M. Coughlin, R. X. Adhikari, and E. Katsavounidis, *Physical Review Research* **2** (2020), 10.1103/physrevresearch.2.033066.
- [36] H. Yu and R. X. Adhikari, “Nonlinear noise regression in gravitational-wave detectors with convolutional neural networks,” (2021).
- [37] S. Schmidt, M. Breschi, R. Gamba, G. Pagano, P. Retegno, G. Riemenschneider, S. Bernuzzi, A. Nagar, and W. D. Pozzo, *Physical Review D* **103** (2021), 10.1103/physrevd.103.043020.
- [38] H. Gabbard, C. Messenger, I. S. Heng, F. Tonolini, and R. Murray-Smith, *Nature Physics* **18**, 112 (2021).
- [39] S.-C. Fragkouli, P. Nousi, N. Passalis, P. Iosif, N. Stergioulas, and A. Tefas, “Deep residual error and bag-of-tricks learning for gravitational wave surrogate modeling,” (2022).
- [40] J. Yan, M. Avagyan, R. E. Colgan, D. Veske, I. Bartos, J. Wright, Z. Márka, and S. Márka, *Physical Review D* **105** (2022), 10.1103/physrevd.105.043006.
- [41] A. H. M. et al., *Physical Review Letters* **111** (2013), 10.1103/physrevlett.111.241104.
- [42] P. Ajith *et al.*, *Phys. Rev. Lett.* **106**, 241101 (2011), arXiv:0909.2867 [gr-qc].
- [43] P. Schmidt, F. Ohme, and M. Hannam, *Phys. Rev. D* **91**, 024043 (2015), arXiv:1408.1810 [gr-qc].
- [44] S. Schmidt, M. Breschi, R. Gamba, G. Pagano, P. Retegno, G. Riemenschneider, S. Bernuzzi, A. Nagar, and W. Del Pozzo, *Phys. Rev. D* **103**, 043020 (2021), arXiv:2011.01958 [gr-qc].
- [45] O. Ronneberger, P. Fischer, and T. Brox, “U-net: Convolutional networks for biomedical image segmentation,” (2015).
- [46] J. C. Duchi, E. Hazan, and Y. Singer, *J. Mach. Learn. Res.* **12**, 2121 (2011).
- [47] “Sxs gravitational waveform database: Important information,” <https://data.black-holes.org/waveforms/index.html>, accessed: 2023-08.
- [48] C. Reisswig and D. Pollney, *Classical and Quantum Gravity* **28**, 195015 (2011).
- [49] M. Ruiz, M. Alcubierre, D. Núñez, and R. Takahashi, *General Relativity and Gravitation* **40**, 1705 (2007).
- [50] A. Nagar and L. Rezzolla, *Classical and Quantum Gravity* **23**, 4297 (2006).
- [51] S. Khan, K. Chatziioannou, M. Hannam, and F. Ohme, *Physical Review D* **100** (2019), 10.1103/physrevd.100.024059.
- [52] A. Taracchini, A. Buonanno, Y. Pan, T. Hinderer, M. Boyle, D. A. Hemberger, L. E. Kidder, G. Lovelace, A. H. Mroué, H. P. Pfeiffer, M. A. Scheel, B. Szilágyi, N. W. Taylor, and A. Zenginoglu, *Physical Review D* **89** (2014), 10.1103/physrevd.89.061502.
- [53] J. Blackman, S. E. Field, C. R. Galley, B. Szilágyi, M. A. Scheel, M. Tiglio, and D. A. Hemberger, *Physical Review Letters* **115** (2015), 10.1103/physrevlett.115.121102.
- [54] J. Blackman, S. E. Field, M. A. Scheel, C. R. Galley, D. A. Hemberger, P. Schmidt, and R. Smith, *Physical Review D* **95** (2017), 10.1103/physrevd.95.104023.
- [55] E. W. Leaver, *Proceedings of the Royal Society A: Mathematical, Physical and Engineering Sciences* **402**, 285 (1985).
- [56] M. Maggiore, *Physical Review Letters* **100** (2008), 10.1103/physrevlett.100.141301.
- [57] H. Yang, D. A. Nichols, F. Zhang, A. Zimmerman, Z. Zhang, and Y. Chen, *Physical Review D* **86** (2012), 10.1103/physrevd.86.104006.